

# ActiveFreq: Integrating Active Learning and Frequency Domain Analysis for Interactive Segmentation

Lijun Guo<sup>a</sup>, Qian Zhou<sup>a</sup>, Zidi Shi<sup>a</sup>, Hua Zou<sup>a,\*</sup> and Gang Ke<sup>b</sup>

<sup>a</sup>School of Computer Science, Wuhan University, Wuhan, 430072, China

<sup>b</sup>Dongguan Polytechnic, Dongguan, 523651, China

## ARTICLE INFO

### Keywords:

Active learning  
Interactive medical segmentation  
Fourier transform  
Mask refinement

## ABSTRACT

Interactive segmentation is commonly used in medical image analysis to obtain precise, pixel-level labeling, typically involving iterative user input to correct mislabeled regions. However, existing approaches often fail to fully utilize user knowledge from interactive inputs and achieve comprehensive feature extraction. Specifically, these methods tend to treat all mislabeled regions equally, selecting them randomly for refinement without evaluating each region's potential impact on segmentation quality. Additionally, most models rely solely on spatial domain features, overlooking frequency domain information that could enhance feature extraction and improve performance. To address these limitations, we propose ActiveFreq, a novel interactive segmentation framework that integrates active learning and frequency domain analysis to minimize human intervention while achieving high-quality labeling. ActiveFreq introduces AcSelect, an autonomous module that prioritizes the most informative mislabeled regions, ensuring maximum performance gain from each click. Moreover, we develop FreqFormer, a segmentation backbone incorporating a Fourier transform module to map features from the spatial to the frequency domain, enabling richer feature extraction. Evaluations on the ISIC-2017 and OAI-ZIB datasets demonstrate that ActiveFreq achieves high performance with reduced user interaction, achieving 3.74 NoC@90 on ISIC-2017 and 9.27 NoC@90 on OAI-ZIB, with 23.5% and 12.8% improvements over previous best results, respectively. Under minimal input conditions, such as two clicks, ActiveFreq reaches mIoU scores of 85.29% and 75.76% on ISIC-2017 and OAI-ZIB, highlighting its efficiency and accuracy in interactive medical segmentation.

## 1. Introduction

Deep learning-based automatic segmentation methods have achieved significant success in medical image analysis, delivering high accuracy and efficiency across various clinical applications [1, 2, 3, 4]. However, these methods depend on large-scale annotated datasets and complex architectures to learn patterns. This reliance creates challenges in medical image segmentation, where datasets are often limited, variable, and difficult to annotate. In contrast, interactive segmentation requires minimal user input to refine predictions and produce precise results, even in complex scenarios. With just a few clicks, users can achieve reliable, high-quality outcomes [5, 6]. By incorporating user expertise, interactive methods provide more accurate and robust segmentations, making them especially valuable in clinical settings where precision is essential [7].

Interactive image segmentation research has explored various interaction inputs, including bounding boxes [8, 9], polygons [10], clicks [11], scribbles [12], and their combinations [13]. Among these, click-based approaches stand out due to their simplicity and well-established protocols for training and evaluation. Recent advancements in click-based segmentation have focused on two key aspects: refining segmentation outputs more efficiently and enhancing the performance of backbone networks.

To improve refinement efficiency, several methods have targeted the local adjustment of segmentation masks. Ding

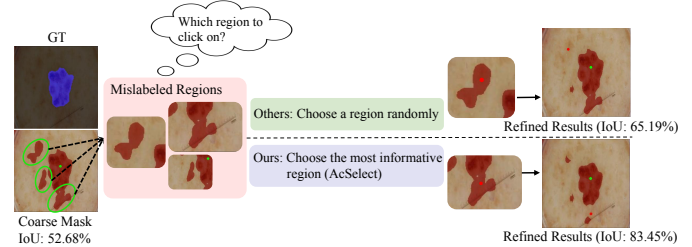


**Figure 1:** Comparison between our proposed method and other methods. While other methods randomly select a mislabeled region to click, our approach uses an active learning selection module (AcSelect) to evaluate all mislabeled areas and select the most valuable one for annotation.

*et al.* [14] propose a dual-stream framework with an interactive shape stream to extract precise boundary information and refine segmentation accuracy through adaptive Gaussian maps. FocalClick [15] and FocusCut [16] refine local regions based on user clicks, preserving details in unaffected areas and iteratively narrowing the refinement scope. Despite their success, these methods typically process new clicks by assigning them through the entire segmentation network, resulting in computational inefficiencies. Addressing this, EMC-Click [17] introduces a lightweight mask correction network that updates coarse masks directly, avoiding the need to rerun the full segmentation pipeline. In parallel, significant efforts have been made to enhance

✉ zouhua@whu.edu.cn (H. Zou)  
ORCID(s):

backbone network performance for interactive segmentation. FCANet [18] incorporates first-click attention mechanisms and click-based loss functions to prioritize user inputs effectively. CGAN [19] leverages adversarial learning to ensure consistency between predictions and ground truths, while CIDN [20] facilitates context interaction across low-level and high-level features to capture detailed structures such as vascular boundaries. These innovations have substantially improved feature representation, segmentation accuracy, and interaction efficiency.

Despite significant advancements in interactive segmentation methods, several challenges persist in scenarios involving complex anatomical structures or pathological cases. Existing methods often require numerous user interactions, with each click providing only marginal improvements in segmentation result. This inefficiency is primarily due to suboptimal handling of mislabeled regions during the refinement process. As illustrated in Fig. 1, after generating a coarse mask and identifying multiple mislabeled regions, most existing approaches treat all regions as equally important and randomly select one for annotation. However, different mislabeled regions vary greatly in their potential to improve the final segmentation. To address this, we define the most informative region as the one whose correction brings the highest performance gain. It typically exhibits high prediction uncertainty, a large number of mislabeled pixels, and strong internal error consistency, where the region's overall feature representation closely aligns with that of the most erroneous pixel. Additionally, existing methods rely heavily on spatial domain features, overlooking the complementary advantages of frequency domain analysis. Frequency domain features are particularly beneficial in medical imaging, as they effectively filter high-frequency noise generated by imaging equipment while preserving critical low-frequency structural information [21, 22]. This capability is essential for accurately capturing fine anatomical structures, such as blood vessels and small lesions, which are often challenging to delineate using spatial domain information alone. The absence of frequency domain analysis significantly limits the ability of current models to achieve precise segmentation.

FCANet [18] demonstrates that indiscriminate treatment of sequential clicks leads to suboptimal segmentation accuracy. Building on the insights of this, we observe that treating all mislabeled regions equally during refinement is similarly suboptimal. While FCANet differentiates the treatment of previously applied clicks by assigning varying weights, our approach focuses on the selective refinement of mislabeled regions that will be clicked in the future, addressing the limitation of random click region selection in FCANet. To address these limitations, we propose **ActiveFreq**, a novel pipeline that combines an active learning selection module, **AcSelect**, and a coarse segmentation backbone, **FreqFormer**. **AcSelect** leverages entropy-based metrics to assess the uncertainty within each mislabeled region, assigning scores to prioritize regions with the highest uncertainty for refinement. This targeted module minimizes

user interactions while maximizing segmentation accuracy. Although most active learning-based methods [23, 24, 25, 26] employ entropy-based metrics for sampling, they typically design a single metric based on individual pixels, without exploring the relationships between pixels or among specific regions. In contrast, our proposed **AcSelect** conducts sampling analysis from three levels: individual pixels, pixel sets, and regions, which endows it with stronger sampling capabilities. Notably, **AcSelect** is designed as a plug-and-play module that can be seamlessly integrated into any CNN-based or Transformer-based backbone, enhancing its versatility and adaptability across different architectures. The goal of **AcSelect** is to intelligently identify and prioritize the most informative regions from coarse segmentation masks. This helps to minimize the user interaction cost while ensuring that each click contributes maximal refinement. **FreqFormer** enhances the segmentation backbone by improving the decoder structure of SegFormer [27]. Specifically, **FreqFormer** incorporates Fourier transform modules to extract frequency domain features, which are then fused with spatial features through a redesigned decoder. It leverages multi-dimensional frequency analysis to capture both global structural patterns and fine-grained details, serving as a robust foundation for subsequent interactive refinements.

In general, our contributions can be summarized as follows:

- We propose **ActiveFreq**, a novel interactive segmentation framework that maintains high segmentation accuracy with a few clicks. To the best of our knowledge, it is the first pipeline that prioritizes mislabeled regions based on their informativeness rather than selecting and refining them randomly.
- We develop **AcSelect**, a lightweight and plug-and-play active learning selection module that uses entropy-based metrics to identify and refine the most informative mislabeled regions, which helps to minimize the user interaction cost while ensuring that each click contributes maximal refinement.
- We introduce **FreqFormer** based on SegFormer [27] that incorporates Fourier transform modules to integrate complementary spatial and frequency domain features, improving segmentation precision for complex anatomical structures.
- **ActiveFreq** achieves state-of-the-art performance with **3.74** NoC@90 on ISIC-2017 [28] and **9.27** NoC@90 on OAI-ZIB [29], surpassing previous best results by 23.5% and 12.8%, respectively, while significantly reducing user clicks required for optimal IoU.

## 2. Related Work

### 2.1. Mask Refinement in Interactive Segmentation

Interactive image segmentation has received significant attention in recent years for its ability to use user input to achieve precise, pixel-level object labeling. Early methods

focus on encoding user clicks as spatial information to guide segmentation. For instance, DIOS [8] converts foreground and background clicks into distance maps, which are concatenated with the input image to provide location-specific guidance. BRS [30] and its extension, f-BRS [31], frame the task as an inference-time optimization problem. BRS refines segmentation by modifying the input image or distance maps, while f-BRS optimizes intermediate layer weights to improve both speed and accuracy. Ding *et al.* [14] propose an interactive shape stream with adaptive Gaussian maps and a probability click loss function for precise boundary extraction and detail sensitivity. RITM [11] enhances robustness by using previous segmentation masks as input, stabilizing predictions with each click. RE-3DLVNet [32] combines 3D segmentation and reinforced quantification with a novel consistency constraint, enabling precise left ventricle volume estimation through refined volume adjustment and accurate anatomical visualization. To further improve efficiency and accuracy, recent methods have explored lightweight architectures and advanced refinement strategies. FocalClick [15] uses a progressive merging mechanism to analyze morphological relationships between previous masks and current predictions, identifying regions to update or preserve. FocusCut [16] adaptively crops click-centered patches from the original image after generating a global prediction, enabling more localized refinements. SimpleClick [33] employs a non-hierarchical Vision Transformer (ViT) with Masked Auto-Encoder (MAE) pre-training, enhancing global feature extraction while reducing computational costs. EMC-Click [17] introduces a lightweight mask correction network that updates the mask iteratively without requiring the full segmentation model to rerun after each click. Finally, CFR-ICL [34] proposes a Cascade-Forward Refinement strategy, allowing iterative refinement during inference without adding extra network modules. Despite recent advances, interactive segmentation methods often treat all mislabeled regions with equal importance, reducing the effectiveness of each click and requiring more user interactions for accurate results. Additionally, these models primarily rely on spatial domain information, overlooking valuable frequency domain features that could enhance robustness by filtering out high-frequency noise and preserving essential structural details.

## 2.2. Active Learning for Semantic Segmentation

Active learning approaches for image segmentation generally fall into two main categories based on annotation strategies: image-level and region-level methods. Image-level methods select samples for annotation by comparing differences between them. For instance, Yang *et al.* [35] develop a framework that uses uncertainty sampling and similarity estimation to select the most representative samples. Ozdemir *et al.* [36] use Bayesian sample querying, combining uncertainty and representativeness in an MMD-optimized latent space to enhance annotation efficiency and segmentation performance in medical imaging. Jin *et al.* [37]

propose a one-shot active learning framework that integrates contrastive self-supervised learning with a diversity-based sampling strategy, significantly reducing annotation costs while maintaining high segmentation accuracy. Gaillochet *et al.* [38] introduce Stochastic Batch Selection, a novel strategy that evaluates uncertainty at the batch level rather than at the individual sample level. Recently, active learning research has increasingly focused on region-level approaches, which enable more precise sample selection. Mackowiak *et al.* [39] assess various strategies, including Random, Entropy, and Vote Entropy, incorporating annotation costs measured by pixels or clicks to improve selection efficiency. Lenczner *et al.* demonstrate that although pixel-wise entropy is a common uncertainty sampling strategy in active learning, it has been shown to be more effective and concise compared to MC Dropout [40], ODIN [41], and ConfidNet [42]. Therefore, many existing uncertainty sampling methods rely on pixel-wise entropy. For instance, DIAL [23] uses the pixel entropy metric derived from softmax output to sample. Similarly, Burmeister *et al.* [24] use pixel entropy sums to select target slices when sampling 2D slices from 3D data. However, these methods neglect which sample or slice contains the most informative regions, which limits its comprehensiveness. RIPU [25] introduces a sample labeling method based on prediction uncertainty (PU), but still relies solely on the sum of pixel entropy throughout the sample without addressing regions requiring specific attention. ViewAL [26] introduces View Entropy Score, which calculates the entropy of each pixel's probability distribution across categories, but it still fails to integrate the surrounding pixels for a holistic analysis. These approaches often fall short by neglecting the holistic inconsistency within the sample and employing metrics that are overly simplistic and lack comprehensiveness, failing to account for the interrelationships and complementarity between sub-regions. In contrast, our proposed AcSelect comprehensively considers three levels: individual pixels, pixel sets, and regions, evaluating from local to global perspectives, which endows it with stronger sampling capabilities.

## 2.3. Frequency Domain Analysis

Recent studies have explored the integration of frequency domain analysis into deep learning, revealing its potential to enhance optimization strategies [43] and generalization capabilities [44]. Zhang *et al.* [45] investigate how frequency aliasing affects the shift-invariance of modern models, and subsequently, AdaBlur [46] applies content-aware low-pass filters during downsampling for anti-aliasing. Rahaman *et al.* [47] and Xu *et al.* [48] identify a phenomenon known as spectral bias (or the frequency principle), where deeper network layers prioritize learning low-frequency components during training. Similarly, Qin *et al.* [49] and Magid *et al.* [50] leverage discrete cosine transform (DCT) coefficients for channel attention mechanisms. FLC [51] highlights the adverse effects of frequency aliasing on model robustness. Recent advancements have utilized frequency components for architectural improvements. Meanwhile,

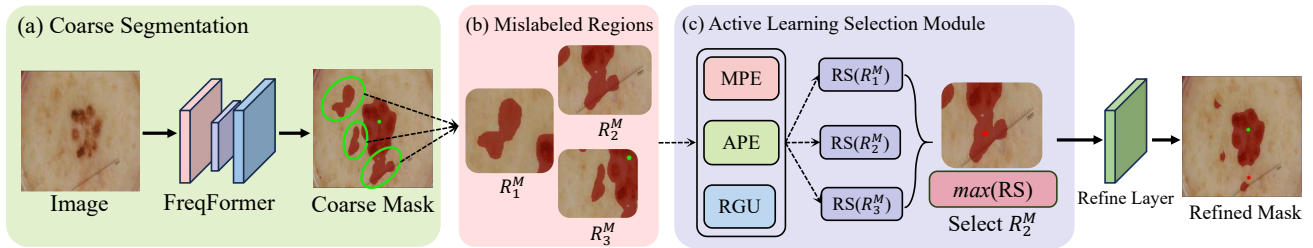


**Figure 2:** The overall pipeline of ActiveFreq. (a) Coarse segmentation is generated using the proposed FreqFormer. (b) Mislabeled regions within the coarse mask. (c) The AcSelect module selects the most informative region for refinement. This process evaluates each mislabeled region using three metrics: Maximum Pixel Entropy (MPE), Average Pixel Entropy (APE), and Regional Group Uncertainty (RGU). A Region Score (RS) is calculated for each region, and the region with the highest score is chosen for further refinement to produce the refined mask.

Huang *et al.* [52] adaptive frequency filters, inspired by the convolution theorem, to act as global token mixers in deep networks. Such approaches enable models to capture non-local features more effectively [52, 53, 54, 55, 56]. Beyond architectural improvements, frequency domain analysis addresses practical challenges in computer vision. Chen *et al.* [57] demonstrate that low-pass filters can suppress high-frequency noise in low-light images, significantly improving instance segmentation performance. Moreover, adversarial attack studies [43, 58, 59] reveal that manipulating high-frequency components severely degrades feature representations. Luo *et al.* [58] show that perturbing high frequencies reduces intra-category similarity, thereby undermining model robustness. These studies demonstrate the effectiveness of frequency domain analysis in various computer vision tasks, motivating us to integrate it into interactive medical image segmentation for enhanced accuracy and efficiency.

### 3. Method

In this section, we present the proposed pipeline ActiveFreq, as illustrated in Fig. 2. In Sec.3.1, we introduce AcSelect, a module for identifying the most informative mislabeled region for annotation, based on three key metrics: maximum pixel entropy (MPE), average pixel entropy (APE), and regional group uncertainty (RGU). In Sec.3.2, we describe FreqFormer in detail, which incorporates a multi-dimensional Fourier transform module into the SegFormer [27] architecture, enabling the network to capture frequency domain information effectively.

To identify all mislabeled regions, we define mislabeled pixels by comparing the initial prediction with the ground truth (GT). If a pixel’s prediction matches the GT, it is considered correct (true), while a mismatch is considered a mislabeled pixel (false). We then employ the concept of connected components, grouping together all contiguous mislabeled pixels. This process involves identifying all connected regions of mislabeled pixels, where each region is defined as a set of pixels that are connected to each other based on a defined connectivity criterion. Once these connected

components are identified, all subsequent operations on the regions are based on these connected subgraphs, enabling targeted refinement and correction of the segmentation results.

#### 3.1. AcSelect using Active Learning

AcSelect is designed to identify the most informative region for annotation by assessing the uncertainty across all mislabeled regions in the coarse segmentation mask. Informative regions are those where correction is likely to yield the greatest performance gain. Specifically, such a region typically satisfies three criteria: (1) high prediction uncertainty, reflecting the model’s low confidence in that area; (2) a large number of mislabeled pixels, indicating a significant concentration of errors; and (3) high error consistency, where the region’s overall feature representation closely aligns with that of the most erroneous pixel, suggesting that the whole region is consistently mislabeled and suitable for effective correction. These properties collectively define the most informative region, which offers the greatest corrective value per interaction. According to these, AcSelect uses three metrics based on pixel entropy: maximum pixel entropy (MPE), average pixel entropy (APE), and regional group uncertainty (RGU). Pixel entropy assesses the model’s confidence by examining the probability distribution across classes for each pixel [60, 61]. High entropy values indicate similar predicted probabilities across classes, which reflects high uncertainty and often highlights areas where the model struggles, making these metrics effective for identifying mislabeled regions [62]. By leveraging MPE, APE, and RGU, AcSelect prioritizes the most uncertain regions for refinement, improving segmentation accuracy with each refinement iteration.

##### 3.1.1. Maximum Pixel Entropy

The maximum pixel entropy (MPE) score estimates pixel-level uncertainty by identifying the highest entropy value within a mislabeled region. This metric reflects the model’s confidence in its prediction for the most uncertain pixel, effectively highlighting regions containing pixels with

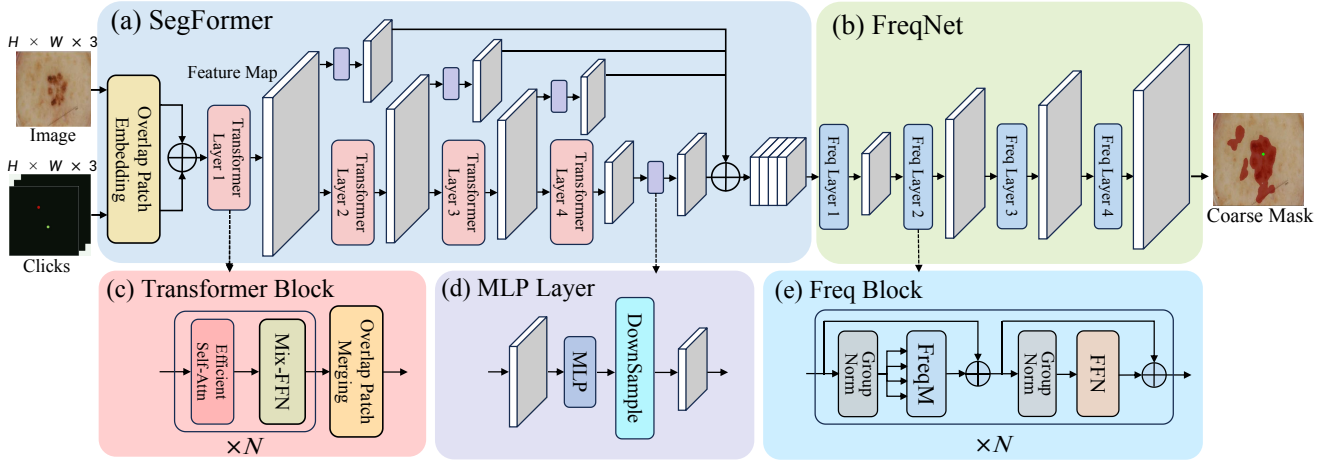


**Figure 3:** The diagram of FreqFormer. (a) SegFormer encoder extracts multi-scale features from the input image and user clicks. (b) FreqNet decoder, composed of four Freq layers, refines these features to produce a coarse mask. (c) Transformer Block architecture, where FFN means feed-forward network. (d) MLP Layer aligns feature maps for final concatenation. (e) Freq Block architecture in the Freq layer, in which FreqM represents the proposed frequency analysis module.

high uncertainty. MPE is defined as:

$$\text{MPE}(R^M) = \max_{i \in R^M} \left[ - \sum_{c=0}^C p(y_i = c) \log p(y_i = c) \right] \quad (1)$$

where  $R^M$  denotes a mislabeled region, and  $p(y_i = c)$  is the predicted probability of pixel  $i$  belonging to class  $c$ .

### 3.1.2. Average Pixel Entropy

While MPE targets the most uncertain pixel, the average pixel entropy (APE) score assesses the overall uncertainty across all pixels within a mislabeled region. APE provides a more holistic measure of prediction uncertainty by averaging the entropy values of all pixels in the region, defined as:

$$\text{APE}(R^M) = - \frac{1}{|R^M|} \sum_{i \in R^M} \sum_{c=0}^C p(y_i = c) \log p(y_i = c) \quad (2)$$

where  $|R^M|$  represents the number of pixels in the mislabeled region  $R^M$ .

### 3.1.3. Regional Group Uncertainty

The regional group uncertainty (RGU) score estimates uncertainty at the region level by leveraging the assumption that pixels within the same region tend to share similar characteristics, such as color or texture [63, 64]. This metric identifies a dominant pixel within a mislabeled region, which exhibits the highest degree of error, and compares it to the average predicted probability of the region. The difference between this dominant pixel and the regional average reflects the inconsistency within the region, providing a measure of uncertainty. RGU is calculated as:

$$\text{RGU}(R^M) = 1 - \log |P_e - \bar{P}| \quad (3)$$

$$P_e = \begin{cases} \max(P_i), & R^M \in FP \\ \min(P_i), & R^M \in FN \end{cases} \quad (4)$$

$$\bar{P} = \frac{1}{|R^M|} \sum_{i \in R^M} \sum_{c=0}^C p(y_i = c) \quad (5)$$

where  $P_e$  is the predicted probability of the pixel with the highest degree of error, and  $\bar{P}$  is the average predicted probability of all pixels within  $R^M$ .  $|R^M|$  represents the number of pixels in the mislabeled region  $R^M$ .  $FP$  and  $FN$  denote false positive and false negative regions, respectively.

### 3.1.4. Mislabeled Region Selection

The selection of mislabeled regions is performed in two steps. First, we calculate the above three metrics for all mislabeled regions in the initial prediction. These scores are then combined using weighted coefficients to ensure balanced contributions from each metric, defining the overall region score (RS) as follows:

$$\text{RS}(R^M) = w_a \cdot \text{MPE} + w_b \cdot \text{APE} + w_c \cdot \text{RGU} \quad (6)$$

In the second step, we select the region with the highest region score, which represents the area with the greatest segmentation uncertainty. This region is prioritized for refinement, as it offers the highest potential for improving segmentation accuracy through targeted manual intervention. The selection process is formalized as:

$$R_{\text{selected}} = \text{argmax}(\text{RS}(R^M)) \quad (7)$$

After selecting the target mislabeled region and performing interactive annotation, the sample with the new click is fed into the refinement layer for further processing.

### 3.2. Network Architecture of FreqFormer

This section introduces the proposed network architecture, FreqFormer, as illustrated in Fig. 3. FreqFormer consists of two main components: the SegFormer encoder [27] and the FreqNet decoder. SegFormer combines a Vision Transformer (ViT) [65] backbone with a lightweight MLP decoder for efficient feature extraction and transformation. The proposed FreqNet enhances segmentation by integrating complementary frequency domain information into spatial domain features.

#### 3.2.1. SegFormer Encoder

As shown in Fig. 3 (a), the SegFormer encodes the input image and the click map into a concatenated feature map for further processing. It consists of four hierarchical transformer layers that use self-attention to capture multi-resolution features. Four lightweight MLP layers unify the feature maps from each stage into a consistent resolution, preparing them for concatenation and subsequent decoding.

#### 3.2.2. FreqNet Decoder

The FreqNet decoder, shown in Fig. 3 (b), is designed to address limitations in existing methods that primarily focus on spatial domain information. Spatial domain features often struggle to distinguish boundaries between objects and backgrounds, while frequency domain features provide complementary information by separating objects based on their frequency components [66]. The FreqNet consists of four Freq layers and each layer comprising  $N$  Freq blocks, with each block progressively refining the features extracted by the SegFormer backbone. As depicted in Fig.3 (e), each Freq block is composed of a sequence of operations: Group Normalization (GN), Frequency Analysis Module (FreqModule), another Group Normalization, and a Feed-Forward Network (FFN). Residual connections are applied after the FreqModule and FFN, allowing the network to retain information from previous layers while refining the features.

#### 3.2.3. Frequency Analysis Module

Fig. 4 shows the details of the Frequency Analysis Module (FreqModule). It processes feature maps to extract both spatial and frequency domain information. Given an input feature map of dimensions  $H \times W \times C$ , the channel dimension is divided uniformly into four parts, producing four sub-feature maps  $\{x_1, x_2, x_3, x_4\}$  of size  $H \times W \times \frac{C}{4}$ . More specifically, the first sub-feature map is processed using a depth-wise convolution (DWConv) to retain spatial domain information. The remaining three sub-feature maps are sequentially processed using 2D Discrete Fourier Transform (2D DFT) and 2D Inverse Discrete Fourier Transform (2D IDFT), extracting frequency domain features. These operations allow the network to capture complementary information that aids in distinguishing object boundaries.

**Depth-wise Separable Convolution (DW Conv).** The first sub-feature map, denoted as  $x_1$ , is processed using depth-wise separable convolution to retain spatial features. This

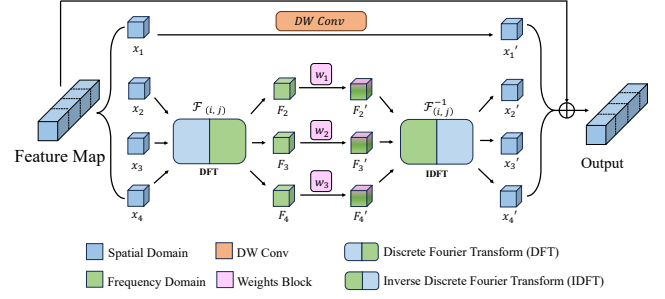


**Figure 4:** The architecture of frequency analysis module (FreqModule). The input feature map is split into four sub-feature maps: one is processed with depth-wise convolution (DW Conv) for spatial information, while the other three pass through 2D Discrete Fourier Transform (DFT) and 2D Inverse DFT (IDFT) for frequency information. The outputs are then concatenated to produce the final result.

operation is expressed as:

$$x_1' = \text{DWConv}(x_1) \quad (8)$$

**2D Discrete Fourier Transform (2D DFT).** The remaining three sub-feature maps,  $x_2, x_3$ , and  $x_4$ , are transformed into the frequency domain using 2D DFT to capture spatial and cross-channel frequency information. Each sub-feature map undergoes 2D DFT along different dimension pairs, *i.e.*, along the height  $H$  and width  $W$  for  $x_2$ , along the height  $H$  and channel  $C$  for  $x_3$ , and along the width  $W$  and channel  $C$  for  $x_4$ :

$$F_2(u, v, c) = \sum_{x=0}^{H-1} \sum_{y=0}^{W-1} x_2(x, y, c) \cdot e^{-j2\pi(\frac{ux}{H} + \frac{vy}{W})} \quad (9)$$

$$F_3(u, y, v) = \sum_{x=0}^{H-1} \sum_{c=0}^{\frac{C}{4}-1} x_3(x, y, c) \cdot e^{-j2\pi(\frac{ux}{H} + \frac{vc}{4})} \quad (10)$$

$$F_4(x, u, v) = \sum_{y=0}^{W-1} \sum_{c=0}^{\frac{C}{4}-1} x_4(x, y, c) \cdot e^{-j2\pi(\frac{uy}{W} + \frac{vc}{4})} \quad (11)$$

where  $(x, y, c)$  is the coordinates in the spatial domain  $(u, v, c)$ ,  $(u, y, v)$  and  $(x, u, v)$  are the coordinates in the frequency domain.  $j$  is an imaginary unit.

**2D Inverse Discrete Fourier Transform (2D IDFT).** Each frequency-transformed sub-feature map is assigned a unique weight  $w_i$ , applied to the corresponding 2D DFT output to adjust its contribution. We then perform 2D IDFT to convert these frequency domain features back to the spatial domain as follows:

$$F_i' = w_i \cdot F_i, \quad i = 2, 3, 4 \quad (12)$$

$$x_i' = \mathcal{F}_{2D}^{-1}(F_i'), \quad i = 2, 3, 4 \quad (13)$$

where  $w_i$  represents the unique weights for each feature map, and  $\mathcal{F}_{2D}^{-1}$  denotes the 2D IDFT operation. On the  $(H, W)$  dimensions, the 2D IDFT is given by:

$$f(x, y, c) = \frac{1}{H \cdot W} \sum_{u=0}^{H-1} \sum_{v=0}^{W-1} F_1(u, v, c) \cdot e^{j2\pi\left(\frac{ux}{H} + \frac{vy}{W}\right)} \quad (14)$$

For 2D IDFT transformations along  $(H, C)$  dimensions and  $(W, C)$  dimensions, a similar operation is used with corresponding summation indices.

Finally, the processed sub-feature maps  $x'_1, x'_2, x'_3$ , and  $x'_4$  are concatenated along the channel dimension to form the output feature map  $x'$ , matching the shape of the original input feature map and serving as the output of the FreqModule.

### 3.3. Refinement Process

In the refinement process, following FocalClick [15], we employ a series of methods to ensure that previously correctly segmented regions remain unaffected. First, we assign smaller weights to correctly segmented regions or completely exclude them from updates, reducing their influence during refinement. This allows the model to focus on correcting the areas that need attention. Additionally, we leverage ROI Align [67], which precisely extract features from regions of interest (ROI) in the feature map, ensuring that spatial information is preserved without any quantization errors. By using bilinear interpolation instead of fixed grid pooling, ROI Align accurately aligns the features with the original object boundaries. This method guarantees that the correctly segmented regions remain unaffected during refinement, as it selectively focuses on the areas requiring adjustment, without altering the previously accurate segmentation, which maintains the integrity of correctly segmented areas.

The Refine Layer is the last module in the refinement process, which decodes the output of FreqFormer and maps it to the original size. Following FocalClick [15], the specific structure is as follows:

$$\text{output} = \text{XConvBlock}(\text{ConvBlock}(x')) \quad (15)$$

where  $x'$  represents the output of the FreqFormer. ConvBlock consists of a convolutional layer followed by batch normalization and a ReLU activation function (Conv + BN + ReLU). XConvBlock is composed of a  $3 \times 3$  convolutional layer, a  $1 \times 1$  convolutional layer, batch normalization, and a ReLU activation function ( $3 \times 3$  Conv +  $1 \times 1$  Conv + BN + ReLU).

## 4. Experiments

To show the effectiveness of ActiveFreq, we compare our method with seven state-of-the-art interactive segmentation approaches, including CDNet [68], RITM [11], iSegFormer [69], FocalClick [15], SimpleClick [33], GP-CIS [70], and GraCo [71]. For a more comprehensive comparison, we also introduce two variants of our model to validate the flexibility and adaptability of the proposed

**Table 1**

Configuration of the FreqFormer architecture, including transformer layers in the encoder and Freq layers in the decoder. Embed dim means the channel  $C$  of feature maps, and attn heads are the number of heads in self-attention.

Layer Type	Layer Index	Embed Dim	Attn Heads	Block Num
Transformer	1	32	1	2
	2	64	2	2
	3	128	4	2
	4	256	8	2
FreqLayer	1	256	-	1
	2	128	-	1
	3	64	-	1
	4	32	-	1

AcSelect module. In Variant-1, AcSelect is directly applied to FocalClick [15] based on HRNet-18 [72], while Variant-2 applies AcSelect to FocalClick with SegFormerB0 [27] as the backbone.

### 4.1. Experimental setups

**Datasets.** We conduct experiments on two datasets: ISIC-2017 [28] and OAI-ZIB [29]. ISIC-2017 is a large-scale dataset of dermoscopy images from the International Skin Imaging Collaboration (ISIC), containing 2000 images for training, 600 for validation, and 150 for testing. The OAI-ZIB dataset consists of 507 3D MRI images with annotations for the femur, tibia, patella, and tibial cartilage. Following iSegFormer [69], we focus on cartilage segmentation, selecting three specific slices (slices 40, 80, and 120) from each image, resulting in 1521 training slices, 150 validation slices, and 150 testing slices.

**Evaluation Metrics.** Consistent with previous studies [33, 11], we evaluate performance using the Number of Clicks (NoC) required to reach predefined Intersection-over-Union (IoU) thresholds of 80%, 85% and 90%, denoted as NoC@80, NoC@85, and NoC@90, respectively. The maximum number of clicks per instance is capped at 20. Additionally, following SimpleClick [33], we report the mean IoU at a fixed number of clicks (mIoU@ $k$ ) to assess segmentation quality under limited user input.

**Implementation Details.** The encoder of our FreqFormer mainly consists of four transformer layers while the decoder contains four Freq layers. The detailed configurations are presented in Tab. 1. Input images are resized to  $224 \times 224$  for ISIC-2017 [28] and  $384 \times 384$  for OAI-ZIB [29]. For the Region Score (RS) computation, the weights are set as follows:  $w_a = 0.35$ ,  $w_b = 0.35$ , and  $w_c = 0.30$ . We train all models for 120 epochs, with an initial learning rate of  $5e-5$ , decaying to  $5e-6$  after 50 epochs. Batch size is set to 16 for FreqFormer. All experiments are conducted on two NVIDIA RTX 4090 GPUs using Pytorch. Data augmentation techniques are employed to avoid overfitting, including random resizing (0.75 to 1.25 scale), flipping, rotation, brightness adjustment, and cropping. The Adam [73] optimizer with  $\beta_1 = 0.9$  and  $\beta_2 = 0.999$  is adopted during training.

**Table 2**

Quantitative comparison of NoC performance with other methods. Results are reported on two medical benchmarks: ISIC-2017 [28] and OAI-ZIB [29]. The best scores are highlighted in bold, and the second-best are underlined.

Method	Venue	Backbone	ISIC-2017 [28]			OAI-ZIB [29]		
			NoC@80	NoC@85	NoC@90	NoC@80	NoC@85	NoC@90
CDNet [68]	ICCV2021	ResNet-34	4.18	5.18	6.79	6.20	8.56	9.61
RITM [11]	ICIP2022	HRNet-18	2.90	3.70	5.69	8.41	14.53	19.25
RITM [11]	ICIP2022	HRNet-32	5.99	7.77	11.28	8.93	14.84	19.56
iSegFormer [69]	MICCAI2022	HRNet-32	2.73	3.66	5.91	8.37	12.99	18.81
FocalClick [15]	CVPR2022	HRNet-18	2.83	3.63	<u>5.01</u>	5.75	8.17	9.83
FocalClick [15]	CVPR2022	HRNet-32	4.20	5.52	8.34	6.11	7.92	<u>9.39</u>
GPCIS [70]	CVPR2023	ResNet-50	<b>2.24</b>	<u>3.23</u>	5.52	<u>4.84</u>	<b>7.20</b>	9.69
Variant-1 (Ours)	-	HRNet-18	<u>2.27</u>	<b>2.86</b>	<b>4.08</b>	<b>4.75</b>	<u>7.34</u>	<b>9.35</b>
iSegFormer [69]	MICCAI2022	Swin-B	2.91	3.93	6.61	16.37	18.41	19.88
iSegFormer [69]	MICCAI2022	Swin-L	10.03	11.56	13.96	19.94	20+	20+
FocalClick [15]	CVPR2022	SegFormerB0	2.27	3.05	5.13	5.54	8.35	9.66
SimpleClick [33]	ICCV2023	ViT-B	2.32	2.98	4.89	7.68	13.23	19.29
SimpleClick [33]	ICCV2023	ViT-L	2.86	3.71	5.89	7.34	13.23	19.30
GPCIS [70]	CVPR2023	SegFormerB0	2.18	2.95	4.29	5.23	<u>7.67</u>	9.66
GraCo [71]	CVPR2024	ViT-B	2.23	2.84	4.16	5.59	7.82	<u>9.41</u>
GraCo [71]	CVPR2024	ViT-L	2.31	2.97	4.34	5.25	7.79	9.42
Variant-2 (Ours)	-	SegFormerB0	<u>1.90</u>	<u>2.52</u>	<u>4.09</u>	<u>4.58</u>	7.71	9.64
ActiveFreq (Ours)	-	FreqFormer	<b>1.74</b>	<b>2.21</b>	<b>3.74</b>	<b>4.57</b>	<b>6.91</b>	<b>9.27</b>

## 4.2. Comparison with state-of-the-art approaches

### 4.2.1. Quantitative Analysis

**NoC Performance.** As shown in Tab. 2, ActiveFreq establishes new state-of-the-art results on both the ISIC-2017 [28] and OAI-ZIB [29] datasets. Specifically, it achieves 3.74 NoC@90 on ISIC-2017, surpassing the previous best method, GraCo-ViT-B [71] (4.16 NoC@90) by 10.1%, and 9.27 NoC@90 on OAI-ZIB, improving upon FocalClick-HRNet-32 [15] (9.39 NoC@90) by 0.12 clicks. These results demonstrate ActiveFreq’s capability to reduce user interactions while maintaining superior segmentation accuracy. The superiority of ActiveFreq stems from AcSelect’s ability to prioritize informative mislabeled regions and FreqFormer’s integration of spatial and frequency domain features for enhanced feature representation.

The effectiveness of AcSelect is further validated by the performance of the two model variants. Variant-1 (AcSelect-HRNet18) achieves 4.08 NoC@90 on ISIC-2017 and 9.35 NoC@90 on OAI-ZIB, compared to 5.01 NoC@90 and 9.83 NoC@90 for the original FocalClick-HRNet18 [15], highlighting a substantial improvement. Similarly, Variant-2 (AcSelect-SegFormerB0) achieves 4.09 NoC@90 on ISIC-2017 and 9.64 NoC@90 on OAI-ZIB, outperforming the original FocalClick-SegFormerB0 [15], which records 5.13 NoC@90 and 9.66 NoC@90, respectively. These results confirm the adaptability and robustness of AcSelect across CNN-based and Transformer-based backbones, demonstrating its capability to optimize the refinement process and enhance segmentation accuracy.

The performance gap between ActiveFreq and its variants (Variant-1 and Variant-2) underscores the additional advantages introduced by FreqFormer. On the ISIC-2017 dataset, ActiveFreq achieves 2.21 NoC@85, demonstrating a 22.73% and 12.31% reduction in the number of clicks required to reach the convergence threshold compared to Variant-1 (AcSelect+HRNet18) and Variant-2 (AcSelect+SegFormerB0), respectively. Similarly, on the OAI-ZIB dataset, ActiveFreq achieves 6.91 NoC@85, achieving a 5.86% and 10.38% reduction in click requirements compared to Variant-1 and Variant-2, respectively. These improvements highlight the effectiveness of FreqFormer in integrating spatial and frequency domain features, enabling more comprehensive feature extraction and enhanced segmentation accuracy, particularly in challenging scenarios involving complex anatomical structures or low-contrast regions.

**User Intervention.** To evaluate the effectiveness of AcSelect under limited user interactions, Fig.5 illustrates the mIoU@2 scores on the ISIC-2017[28] and OAI-ZIB [29] datasets. On ISIC-2017 (Fig.5(a)), variant-2 (AcSelect-SegFormerB0) achieves the highest mIoU of 85.29%, surpassing the second-best method, GPCIS-SegFormerB0 [70] (83.07%), by 2.22%. Similarly, on OAI-ZIB (Fig.5(b)), variant-1 reaches an mIoU@2 of 75.76%, outperforming the next-best method, RITM-HRNet-32 [11] (74.28%), by 1.48%. These results underscore the efficiency of AcSelect in achieving superior segmentation accuracy with minimal user input.

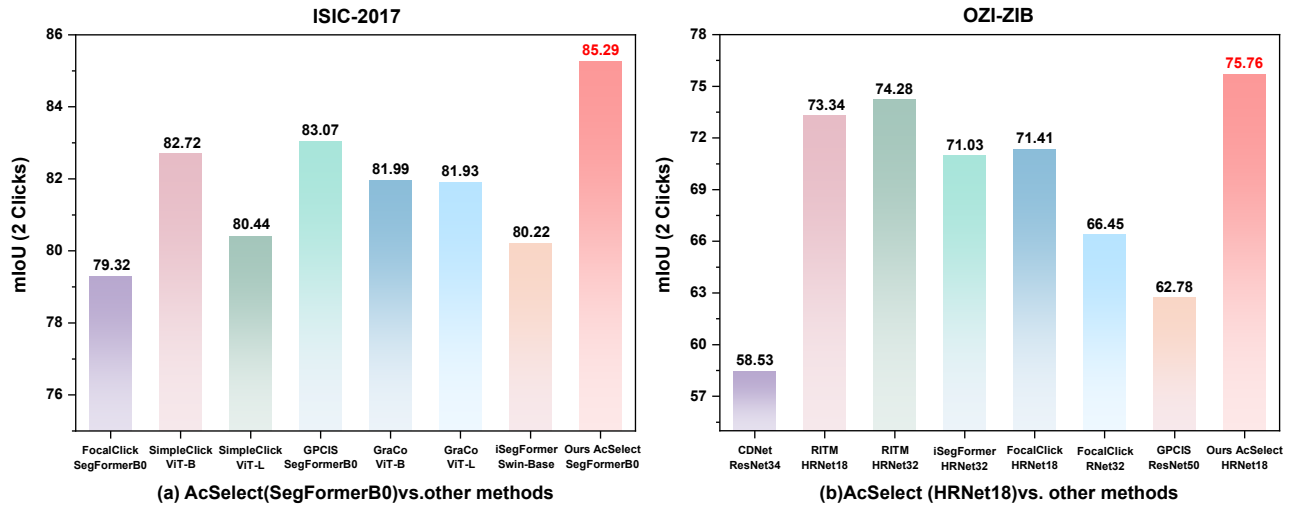


**Figure 5:** Comparison of mIoU@2 performance between our proposed AcSelect and other state-of-the-art methods on two datasets: (a) Transformer-based approaches on ISIC-2017 [28] and (b) CNN-based methods on OAI-ZIB [29].

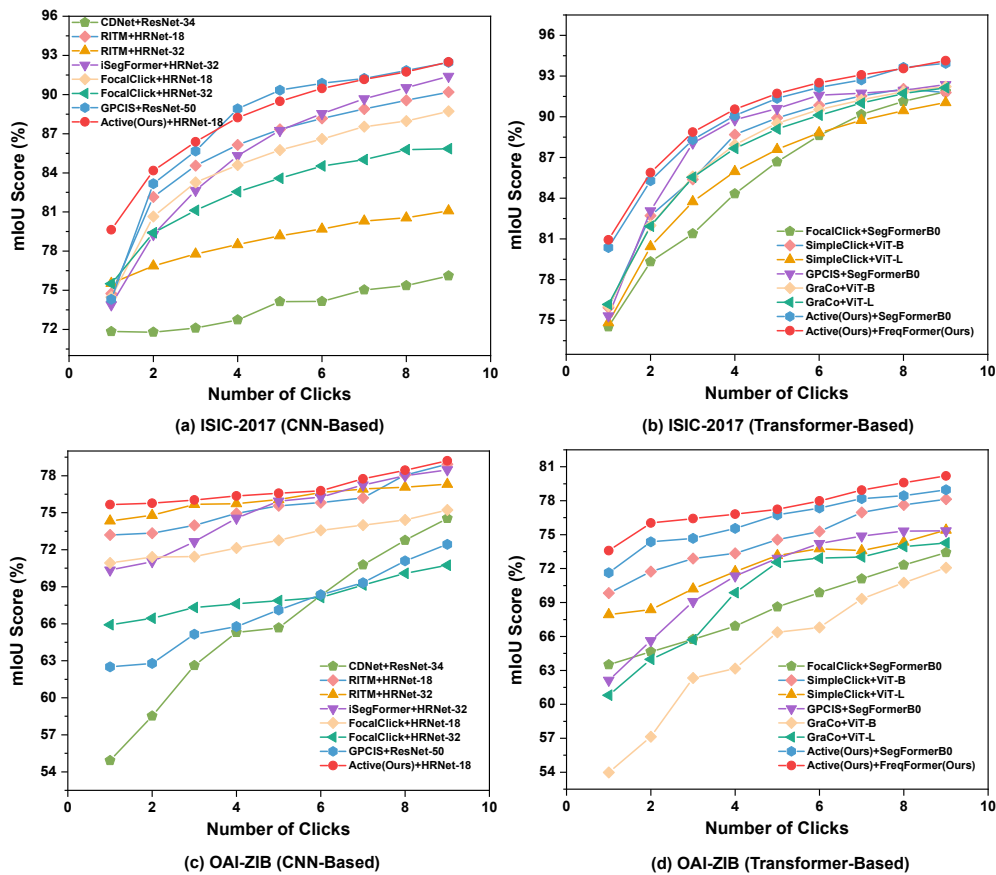


**Figure 6:** mIoU scores with varying numbers of user clicks on two medical datasets. (a) and (b) are CNN-based methods and Transformer-based methods on ISIC-2017 [28]. (c) and (d) show CNN-based and Transformer-based models on OAI-ZIB [29].

Fig. 6 offers a comprehensive analysis of mIoU performance across varying numbers of user clicks, highlighting the convergence efficiency of different methods. On

both ISIC-2017[28] and OAI-ZIB [29] datasets, ActiveFreq consistently requires fewer clicks to achieve comparable or superior performance compared to competing approaches. For instance, on ISIC-2017, ActiveFreq surpasses

**Table 3**

Computation comparison for model parameters, FLOPs, and speed (measured by seconds per click). The best scores are highlighted in bold, and the second-best are underlined.

Backbone	Params/M	FLOPs/G	SPC/ms
ResNet34 [74]	23.47	113.60	<b>34</b>
Resnet50 [74]	40.36	78.82	331
HRNet18 [72]	10.03	30.99	56
HRNet32 [72]	30.95	83.12	86
Swin-Base [75]	87.44	138.21	<u>36</u>
Swin-Large [75]	195.90	302.78	44
ViT-Base [76]	96.46	42.44	54
ViT-Large [76]	322.18	133.22	86
SegFormerB0 [27]	<b>3.72</b>	<b>1.75</b>	37
SegFormerB3 [27]	45.66	24.75	53
FreqFormer (Ours)	<u>9.20</u>	<u>2.67</u>	46

90% mIoU with only four clicks, while methods such as SimpleClick [33] and FocalClick [15] need eight or more clicks to reach similar levels. Likewise, on OAI-ZIB, ActiveFreq achieves 78% mIoU with just six clicks, outperforming other methods that require additional user interactions to reach comparable performance. These findings highlight the rapid convergence of ActiveFreq, making it a robust and efficient choice for interactive segmentation tasks.

**Computational Analysis.** Tab. 3 shows a comparison of computational requirements with respect to model parameters, FLOPs, and speed. For fair comparison, we evaluate all the models on the same benchmark (*i.e.* FocalClick) and using the same computer (GPU: NVIDIA RTX4090, CPU: Intel(R) Xeon(R) Silver). By default, our method takes images of size 448×448 as the fixed input. According to the table, we observe that our proposed FreqFormer achieves the best performance while maintaining a lightweight architecture with a minimal number of parameters (9.20 M) and computational complexity (2.67 G).

#### 4.2.2. Visualization Analysis

Fig. 7 presents qualitative comparisons of segmentation results on the ISIC-2017[28] dataset, highlighting both the segmentation performance and the effectiveness of AcSelect in determining optimal click regions.

The green points indicate positive clicks, while the red points denote negative clicks. Unlike other methods that often randomly select a mislabeled region and place clicks arbitrarily, ActiveFreq, guided by AcSelect, prioritizes the most informative mislabeled regions for user interactions. This targeted selection ensures that each click contributes maximally to refining segmentation quality. It can be seen that clicks of ActiveFreq are strategically placed near regions of high uncertainty or along critical edges, resulting in more precise and complete segmentations. In contrast, GraCo [71] and SimpleClick [33] often distribute clicks in less impactful regions, leading to fragmented or incomplete masks.

**Table 4**

Ablation study results of AcSelect. We use ActiveFreq (AcSelect with FreqFormer) trained on the ISIC-2017 [28] and OAI-ZIB [29] datasets. The experiments incrementally added the three key metrics (MPE, APE, and RGU) to assess their individual and combined contributions to segmentation performance. Results are reported in terms of NoC@85 and NoC@90.

MPE	APE	RGU	ISIC-2017 [28]		OAI-ZIB [29]	
			NoC@85	NoC@90	NoC@85	NoC@90
			3.03	5.11	8.31	9.62
✓			2.75	4.62	7.83	9.49
✓	✓		2.43	4.19	7.37	9.37
✓	✓	✓	<b>2.21</b>	<b>3.74</b>	<b>6.91</b>	<b>9.27</b>

In the last row of Fig. 7, ActiveFreq demonstrates its ability to handle complex boundaries by aligning closely with the ground truth after just five clicks, achieving an IoU of 82.30%. iSegFormer [69], FocalClick [15], and SimpleClick [33] show many False Positive regions, as their click placement fails to adequately address key segmentation errors. This highlights the advantage of AcSelect’s active learning approach in optimizing click allocation.

In addition, Fig. 8 presents the results of the ActiveFreq on the ISIC-2017 [28] dataset, illustrating how incremental user clicks improve performance on four distinct samples. As the number of clicks increases from 1 to 10, the mIoU score significantly improves across all samples, highlighting the model’s ability to refine segmentation with few user interaction. Notably, ActiveFreq achieves a near 90% mIoU score by the seventh click, demonstrating the superiority and effectiveness of the AcSelect strategy in selecting the most informative mislabeled regions.

### 4.3. Ablation Study

We conduct ablation studies to verify the effectiveness of key components in AcSelect and FreqModule on the ISIC-2017 [28] and OAI-ZIB [29] datasets.

#### 4.3.1. AcSelect

Tab. 4 presents the ablation results for AcSelect, where we assess the contributions of its three key metrics: maximum pixel entropy (MPE), average pixel entropy (APE), and regional group uncertainty (RGU), by progressively incorporating them into the model.

Without any metrics, the NoC@90 on ISIC-2017 [28] and OAI-ZIB [29] are 5.11 and 9.62, respectively. Adding MPE reduces NoC@90 to 4.62 and 9.49, confirming its effectiveness in targeting the most uncertain pixels and refining localized errors. Including APE further lowers NoC@90 to 4.19 and 9.37, demonstrating its ability to capture overall uncertainty and balance the model’s focus. Finally, adding RGU achieves the best results, with NoC@90 decreasing to 3.74 and 9.27, showcasing its capacity to enhance regional consistency and refine uniformly uncertain areas.

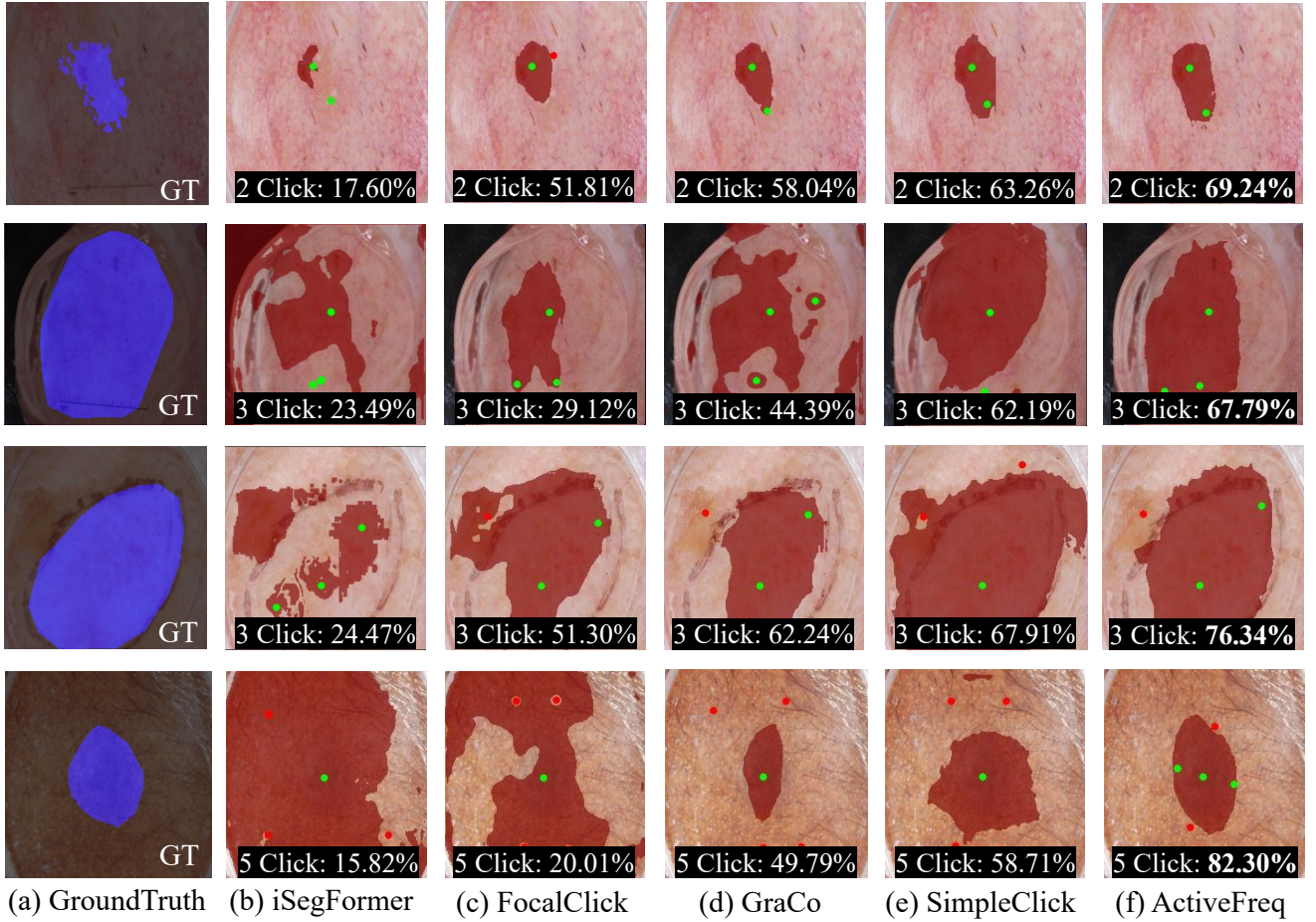


**Figure 7:** Qualitative results on ISIC-2017 [28]. Each row shows (a) ground truth, and segmentation results for (b) iSegFormer [69] using Swin-B, (c) FocalClick [15] with SegFormerB0, (d) GraCo [71] based on ViT-B, (e) SimpleClick [33] with SegFormerB0, (f) the proposed ActiveFreq. Green points indicate positive clicks and red points indicate negative clicks. The red masks represent segmentation results, with numerical values indicating the Intersection over Union (IoU) between the predicted mask and the ground truth.

From these improvements, MPE provides the most significant initial gain by addressing localized uncertainty, making it essential for immediate refinement. APE complements MPE by accounting for broader uncertainty across regions, contributing further gains. While RGU has a smaller standalone impact, it is crucial when combined with MPE and APE, ensuring consistent and robust predictions. These results demonstrate that each metric contributes uniquely and complements the others in enhancing segmentation performance.

Furthermore, to demonstrate the effectiveness of AcSelect’s sampling strategy, we conducted a comparative analysis against Random Sampling, Entropy-Based Sampling, and Least Confidence Sampling. Tab. 5 presents the results of the sampling strategy ablation study, comparing Random Sampling, Entropy-Based Sampling, Least Confidence Sampling, and our proposed AcSelect method on the ISIC-2017 and OAI-ZIB datasets. The results indicate that AcSelect consistently achieves the best performance across both datasets, demonstrating its superior ability to select the most

informative samples for annotation. Notably, compared to Random Sampling, AcSelect reduces NoC@85 by 27.06% on ISIC-2017 and 16.83% on OAI-ZIB, highlighting its efficiency in minimizing the number of clicks required to reach the convergence threshold. Although entropy and least confidence improve performance in random sampling, AcSelect significantly outperforms them, further validating its effectiveness in enhancing interactive segmentation through optimized sample selection.

#### 4.3.2. FreqModule

Tab. 6 presents the ablation results for the FreqModule, where 2D DFT transformations ( $F_{(H,W)}$ ,  $F_{(H,C)}$ , and  $F_{(W,C)}$ ) are progressively added to evaluate their contributions. Without any transformations, the NoC@90 values on ISIC-2017 [28] and OAI-ZIB [29] are 5.22 and 9.73, respectively. Each transformation individually improves performance, with all three combined achieving the best results: reducing NoC@90 to 3.74 on ISIC-2017 [28] and 9.27 on OAI-ZIB [29].

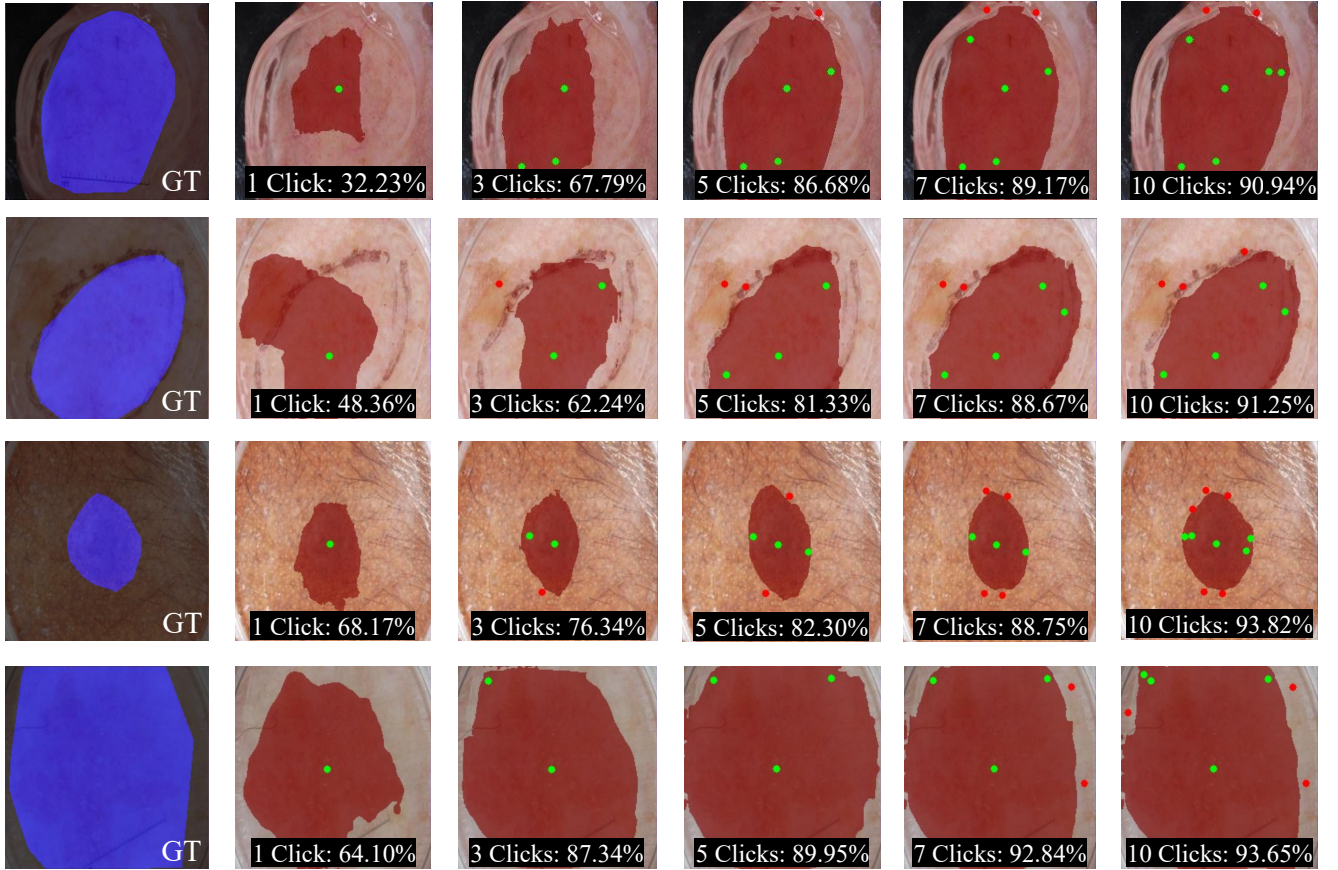


**Figure 8:** Visualization of the mIoU performance for interactive segmentation on four different medical samples using our proposed ActiveFreq with varying click counts. The results demonstrate how the performance improves as the number of clicks increases from 1 to 10.

**Table 5**

Ablation study results on the sampling strategy. This table compares different active learning sampling strategies, including Random Sampling, Entropy-Based Sampling, Least Confidence Sampling. The best results are highlighted in bold.

Sampling Strategy	ISIC-2017		OAI-ZIB	
	NoC@85	NoC@90	NoC@85	NoC@90
Random	3.03	5.11	8.31	9.62
Entropy	2.71	4.68	7.85	9.50
Least Confidence	2.69	4.45	7.72	9.45
AcSelect (Ours)	<b>2.21</b>	<b>3.74</b>	<b>6.91</b>	<b>9.27</b>

The results indicate that each transformation plays a crucial role in improving segmentation precision by capturing complementary information. The  $F_{(H,W)}$  transformation filters high-frequency noise while preserving low-frequency structural patterns, essential for delineating global segmentation boundaries. The  $F_{(H,C)}$  and  $F_{(W,C)}$  transformations enrich contextual understanding by capturing correlations between feature channels and spatial dimensions, which highlight variations in texture and intensity across regions.

**Table 6**

Ablation study results on the FreqModule. We use ActiveFreq (AcSelect with FreqFormer) trained on ISIC-2017 [28] and OAI-ZIB [29]. Experiments include progressively adding 2D DFT transformations ( $F_{(H,W)}$ ,  $F_{(H,C)}$ , and  $F_{(W,C)}$ ) to evaluate their effectiveness.

$F_{(H,W)}$	$F_{(H,C)}$	$F_{(W,C)}$	ISIC-2017 [28]		OAI-ZIB [29]	
			NoC@85	NoC@90	NoC@85	NoC@90
			3.14	5.22	8.42	9.73
✓			2.85	4.74	7.94	9.61
✓	✓		2.52	4.28	7.48	9.48
✓	✓	✓	<b>2.21</b>	<b>3.74</b>	<b>6.91</b>	<b>9.27</b>

The similar magnitude of improvement across all dimensions underscores their complementary roles, collectively enabling the FreqModule to integrate multi-dimensional frequency information effectively. This integration enhances feature representation, reduces user interactions, and leads to robust segmentation performance.

#### 4.3.3. Wavelet Transform vs. Fourier Transform

To further investigate the impact of frequency domain transformations on segmentation performance, we conducted an ablation study by replacing the Fourier Transform

**Table 7**

Ablation study results on the Frequency Module. This table presents a comparison between Fourier Transform (FT) and Wavelet Transform (WT) in the frequency module across the ISIC-2017 and OAI-ZIB datasets. While WT demonstrates some capability in frequency domain representation, FT consistently outperforms WT across all metrics. The better results are highlighted in bold.

Frequency Module	ISIC-2017		OAI-ZIB	
	NoC@85	NoC@90	NoC@85	NoC@90
Wavelet Transform	2.66	3.83	7.09	9.40
Fourier Transform	<b>2.21</b>	<b>3.74</b>	<b>6.91</b>	<b>9.27</b>

(FT) with the Wavelet Transform (WT) in our method. Tab. 7 indicates that although WT enables multi-scale analysis by decomposing features into different frequency bands with spatial localization, FT outperforms WT in capturing global contextual information, leading to better overall segmentation performance. Although WT shows some advantages in fine-structure segmentation and complex textures, it falls short in maintaining global consistency. Based on these findings, we retain FT as the frequency transformation in our approach.

## 5. Limitations

While ActiveFreq demonstrates significant advancements in interactive segmentation, some limitations remain.

First, AcSelect analyzes mislabeled regions individually, potentially missing interactions between regions. The grouping and collectively analyzing regions could improve efficiency by focusing on areas that contribute most to global segmentation accuracy. Second, the FreqModule applies 2D Discrete Fourier Transform (2D DFT) operations across height-width, height-channel, and width-channel dimensions, capturing pairwise frequency information but missing interactions across all dimensions. Future work could explore 3D Discrete Fourier transform (3D DFT) for holistic frequency feature extraction and investigate adaptive weighting or learnable filters to better integrate frequency features and improve segmentation performance.

## 6. Conclusions

In this work, we propose **ActiveFreq**, an interactive image segmentation framework that reduces human intervention while maintaining high segmentation performance. ActiveFreq addresses two key limitations of existing methods: the uniform treatment of all mislabeled regions and the lack of frequency domain analysis. To overcome these challenges, we introduce **AcSelect**, an active learning selection module that prioritizes the most informative mislabeled regions, optimizing refinement efficiency and minimizing user interactions. Additionally, we develop **FreqFormer**, a segmentation network that integrates spatial and frequency domain features using Fourier transform modules,

enhancing feature representation and segmentation accuracy. Extensive experiments on the ISIC-2017 [28] and OAI-ZIB [29] datasets validate the effectiveness of ActiveFreq. Our method achieves state-of-the-art performance, with NoC@90 values of 3.74 on ISIC-2017 and 9.27 on OAI-ZIB. These results demonstrate the great potential of ActiveFreq to advance interactive segmentation and contribute to the development of medical image analysis algorithms.

## CRedit authorship contribution statement

**Lijun Guo:** Methodology, Software, Writing - Original draft preparation. **Qian Zhou:** Writing - Review and editing. **Zidi Shi:** Methodology, Software. **Hua Zou:** Conceptualization of this study, Methodology, Writing - Review and editing, Supervision. **Gang Ke:** Review and editing.

## Declaration of competing interest

The authors declare that they have no competing financial interests or personal relationships that could influence the work reported in this paper.

## Acknowledgments

This work was supported in part by Key Research and Development Program of Hubei Province (2022BCA009); Bingtuan Science and Technology Program (2022DB005); Dongguan Science and Technology of Social Development Program (20231800935472). (Corresponding author: Hua Zou.)

## Data availability

The study used publicly available datasets, including ISIC-2017 (available at <https://challenge.isic-archive.com/data/#2017>) and OAI-ZIB (available at <https://drive.google.com/drive/foIders/1B6y1nNBnWU09EhxvjaTdp1XGjc1T6wUk>).

## References

- [1] Risheng Wang, Tao Lei, Ruixia Cui, Bingtao Zhang, Hongying Meng, and Asoke K Nandi. Medical image segmentation using deep learning: A survey. *IET image processing*, 16(5):1243–1267, 2022.
- [2] Dinggang Shen, Guorong Wu, and Heung-Il Suk. Deep learning in medical image analysis. *Annual review of biomedical engineering*, 19(1):221–248, 2017.
- [3] Yuncong Feng, Yeming Cong, Shuaijie Xing, Hairui Wang, Zihang Ren, and Xiaoli Zhang. Gcformer: Multi-scale feature plays a crucial role in medical images segmentation. *Knowledge-Based Systems*, 300:112170, 2024.
- [4] Haoyu Zhao, Wenhui Dong, Rui Yu, Zhou Zhao, Bo Du, and Yongchao Xu. Morestyle: relax low-frequency constraint of fourier-based image reconstruction in generalizable medical image segmentation. In *International Conference on Medical Image Computing and Computer-Assisted Intervention*, pages 434–444. Springer, 2024.
- [5] Feng Zhao and Xianghua Xie. An overview of interactive medical image segmentation. *Annals of the BMVA*, 2013(7):1–22, 2013.
- [6] Saleha Masood, Muhammad Sharif, Afifa Masood, Mussarat Yasmin, and Mudassar Raza. A survey on medical image segmentation. *Current Medical Imaging*, 11(1):3–14, 2015.

- [7] Guotai Wang, Maria A Zuluaga, Wenqi Li, Rosalind Pratt, Premal A Patel, Michael Aertsen, Tom Doel, Anna L David, Jan Deprest, Sébastien Ourselin, et al. Deepigeos: a deep interactive geodesic framework for medical image segmentation. *IEEE transactions on pattern analysis and machine intelligence*, 41(7):1559–1572, 2018.
- [8] Ning Xu, Brian Price, Scott Cohen, Jimei Yang, and Thomas S Huang. Deep interactive object selection. In *Proceedings of the IEEE conference on computer vision and pattern recognition*, pages 373–381, 2016.
- [9] Zhiwei Zhang, Yisha Liu, and Weimin Xue. Ms-irtnet: Multistage information interaction network for rgb-t semantic segmentation. *Information Sciences*, 647:119442, 2023.
- [10] David Acuna, Huan Ling, Amlan Kar, and Sanja Fidler. Efficient interactive annotation of segmentation datasets with polygon-rnn++. In *Proceedings of the IEEE conference on Computer Vision and Pattern Recognition*, pages 859–868, 2018.
- [11] Konstantin Sofiiuk, Ilya A Petrov, and Anton Konushin. Reviving iterative training with mask guidance for interactive segmentation. In *2022 IEEE International Conference on Image Processing (ICIP)*, pages 3141–3145. IEEE, 2022.
- [12] Jiajun Wu, Yibiao Zhao, Jun-Yan Zhu, Siwei Luo, and Zhuowen Tu. Milcut: A sweeping line multiple instance learning paradigm for interactive image segmentation. In *Proceedings of the IEEE conference on computer vision and pattern recognition*, pages 256–263, 2014.
- [13] Shiyin Zhang, Jun Hao Liew, Yunchao Wei, Shikui Wei, and Yao Zhao. Interactive object segmentation with inside-outside guidance. In *Proceedings of the IEEE/CVF conference on computer vision and pattern recognition*, pages 12234–12244, 2020.
- [14] Zongyuan Ding, Tao Wang, Quansen Sun, Qiongjie Cui, and Fuhua Chen. A dual-stream framework guided by adaptive gaussian maps for interactive image segmentation. *Knowledge-Based Systems*, 223:107033, 2021.
- [15] Xi Chen, Zhiyan Zhao, Yilei Zhang, Manni Duan, Donglian Qi, and Hengshuang Zhao. Focalclick: Towards practical interactive image segmentation. In *Proceedings of the IEEE/CVF Conference on Computer Vision and Pattern Recognition*, pages 1300–1309, 2022.
- [16] Zheng Lin, Zheng-Peng Duan, Zhao Zhang, Chun-Le Guo, and Ming-Ming Cheng. Focuscut: Diving into a focus view in interactive segmentation. In *Proceedings of the IEEE/CVF Conference on Computer Vision and Pattern Recognition*, pages 2637–2646, 2022.
- [17] Fei Du, Jianlong Yuan, Zhibin Wang, and Fan Wang. Efficient mask correction for click-based interactive image segmentation. In *Proceedings of the IEEE/CVF Conference on Computer Vision and Pattern Recognition*, pages 22773–22782, 2023.
- [18] Zheng Lin, Zhao Zhang, Lin-Zhuo Chen, Ming-Ming Cheng, and Shao-Ping Lu. Interactive image segmentation with first click attention. In *Proceedings of the IEEE/CVF conference on computer vision and pattern recognition*, pages 13339–13348, 2020.
- [19] Gui Yan, Zhang Zhengyan, Chen Zhihua, Zhang Chuang, and Zhang Jin. Cgan: lightweight and feature aggregation network for high-performance interactive image segmentation. *The Visual Computer*, 40(3):2203–2217, 2024.
- [20] Min Zhang, Huibin Wang, Liansheng Wang, Abdu Saif, and Sobia Wassan. Cidn: A context interactive deep network with edge-aware for x-ray angiography images segmentation. *Alexandria Engineering Journal*, 87:201–212, 2024.
- [21] Yu Wang, Guoheng Huang, Zeng Lu, Ying Wang, Xuhang Chen, Xiaochen Yuan, Yan Li, Lijie Ni, and Yingping Huang. Hedn: multi-oriented hierarchical extraction and dual-frequency decoupling network for 3d medical image segmentation. *Medical & Biological Engineering & Computing*, pages 1–25, 2024.
- [22] Guangyi Wei, Jindong Xu, Weiqing Yan, Qianpeng Chong, Haihua Xing, and Mengying Ni. Dual-domain fusion network based on wavelet frequency decomposition and fuzzy spatial constraint for remote sensing image segmentation. *Remote Sensing*, 16(19), 2024.
- [23] Gaston Lenczner, Adrien Chan-Hon-Tong, Bertrand Le Saux, Nicola Luminari, and Guy Le Besnerais. Dial: Deep interactive and active learning for semantic segmentation in remote sensing. *IEEE Journal of Selected Topics in Applied Earth Observations and Remote Sensing*, 15:3376–3389, 2022.
- [24] Josafat-Mattias Burmeister, Marcel Fernandez Rosas, Johannes Hagemann, Jonas Kordt, Jasper Blum, Simon Shabo, Benjamin Bergner, and Christoph Lippert. Less is more: A comparison of active learning strategies for 3d medical image segmentation. *arXiv preprint arXiv:2207.00845*, 2022.
- [25] Binhui Xie, Longhui Yuan, Shuang Li, Chi Harold Liu, and Xinjing Cheng. Towards fewer annotations: Active learning via region impurity and prediction uncertainty for domain adaptive semantic segmentation. In *Proceedings of the IEEE/CVF conference on computer vision and pattern recognition*, pages 8068–8078, 2022.
- [26] Yawar Siddiqui, Julien Valentin, and Matthias Nießner. Viewal: Active learning with viewpoint entropy for semantic segmentation. In *Proceedings of the IEEE/CVF conference on computer vision and pattern recognition*, pages 9433–9443, 2020.
- [27] Enze Xie, Wenhui Wang, Zhiding Yu, Anima Anandkumar, Jose M Alvarez, and Ping Luo. Segformer: Simple and efficient design for semantic segmentation with transformers. *Advances in neural information processing systems*, 34:12077–12090, 2021.
- [28] Matt Berseth. Isic 2017-skin lesion analysis towards melanoma detection. *arXiv preprint arXiv:1703.00523*, 2017.
- [29] Felix Ambellan, Alexander Tack, Moritz Ehlike, and Stefan Zachow. Automated segmentation of knee bone and cartilage combining statistical shape knowledge and convolutional neural networks: Data from the osteoarthritis initiative. *Medical image analysis*, 52:109–118, 2019.
- [30] Won-Dong Jang and Chang-Su Kim. Interactive image segmentation via backpropagating refinement scheme. In *Proceedings of the IEEE/CVF Conference on Computer Vision and Pattern Recognition*, pages 5297–5306, 2019.
- [31] Konstantin Sofiiuk, Ilya Petrov, Olga Barinova, and Anton Konushin. f-brs: Rethinking backpropagating refinement for interactive segmentation. In *Proceedings of the IEEE/CVF Conference on Computer Vision and Pattern Recognition*, pages 8623–8632, 2020.
- [32] Rongjun Ge, Cong Xia, Yuting He, Hailong Sun, Daoqiang Zhang, Guangyu Yang, Wentao Xiang, Jinjun Shi, Limin Luo, Yinsu Zhu, et al. Re-3dlvnet: Refined estimation of the left ventricle volume via interactive 3d segmentation and reinforced quantification. *Knowledge-Based Systems*, 251:109212, 2022.
- [33] Qin Liu, Zhenlin Xu, Gedas Bertasius, and Marc Niethammer. Simpleclick: Interactive image segmentation with simple vision transformers. In *Proceedings of the IEEE/CVF International Conference on Computer Vision*, pages 22290–22300, 2023.
- [34] Shoukun Sun, Min Xian, Fei Xu, Luca Capriotti, and Tiankai Yao. Cfr-icl: Cascade-forward refinement with iterative click loss for interactive image segmentation. In *Proceedings of the AAAI Conference on Artificial Intelligence*, Vol. 38, No. 5, pages 5017–5024, 2024.
- [35] Lin Yang, Yizhe Zhang, Jianxu Chen, Siyuan Zhang, and Danny Z Chen. Suggestive annotation: A deep active learning framework for biomedical image segmentation. In *Medical Image Computing and Computer Assisted Intervention- MICCAI 2017: 20th International Conference, Quebec City, QC, Canada, September 11-13, 2017, Proceedings, Part III 20*, pages 399–407. Springer, 2017.
- [36] Firat Ozdemir, Zixuan Peng, Philipp Fuerstahl, Christine Tanner, and Orcun Goksel. Active learning for segmentation based on bayesian sample queries. *Knowledge-Based Systems*, 214:106531, 2021.
- [37] Qiuye Jin, Mingzhi Yuan, Qin Qiao, and Zhijian Song. One-shot active learning for image segmentation via contrastive learning and diversity-based sampling. *Knowledge-Based Systems*, 241:108278, 2022.
- [38] Mélanie Gaillochet, Christian Desrosiers, and Hervé Lombaert. Active learning for medical image segmentation with stochastic batches. *Medical Image Analysis*, 90:102958, 2023.

- [39] Radek Mackowiak, Philip Lenz, Omair Ghori, Ferran Diego, Oliver Lange, and Carsten Rother. Cereals-cost-effective region-based active learning for semantic segmentation. *arXiv preprint arXiv:1810.09726*, 2018.
- [40] Yarin Gal and Zoubin Ghahramani. Dropout as a bayesian approximation: Representing model uncertainty in deep learning. In *international conference on machine learning*, pages 1050–1059. PMLR, 2016.
- [41] Shiyu Liang, Yixuan Li, and Rayadurgam Srikant. Principled detection of out-of-distribution examples in neural networks. *CoRR*, abs/1706.02690, 1, 2017.
- [42] Charles Corbière, Nicolas Thome, Avner Bar-Hen, Matthieu Cord, and Patrick Pérez. Addressing failure prediction by learning model confidence. *Advances in Neural Information Processing Systems*, 32, 2019.
- [43] Dong Yin, Raphael Gontijo Lopes, Jon Shlens, Ekin Dogus Cubuk, and Justin Gilmer. A fourier perspective on model robustness in computer vision. *Advances in Neural Information Processing Systems*, 32, 2019.
- [44] Haohan Wang, Xindi Wu, Zeyi Huang, and Eric P Xing. High-frequency component helps explain the generalization of convolutional neural networks. In *Proceedings of the IEEE/CVF conference on computer vision and pattern recognition*, pages 8684–8694, 2020.
- [45] Richard Zhang. Making convolutional networks shift-invariant again. In *International conference on machine learning*, pages 7324–7334. PMLR, 2019.
- [46] Xueyan Zou, Fanyi Xiao, Zhiding Yu, Yuheng Li, and Yong Jae Lee. Delving deeper into anti-aliasing in convnets. *International Journal of Computer Vision*, 131(1):67–81, 2023.
- [47] Nasim Rahaman, Aristide Baratin, Devansh Arpit, Felix Draxler, Min Lin, Fred Hamprecht, Yoshua Bengio, and Aaron Courville. On the spectral bias of neural networks. In *International conference on machine learning*, pages 5301–5310. PMLR, 2019.
- [48] Zhiqin John Xu and Hanxu Zhou. Deep frequency principle towards understanding why deeper learning is faster. In *Proceedings of the AAAI conference on artificial intelligence*, volume 35, pages 10541–10550, 2021.
- [49] Zequn Qin, Pengyi Zhang, Fei Wu, and Xi Li. Fcanet: Frequency channel attention networks. In *Proceedings of the IEEE/CVF international conference on computer vision*, pages 783–792, 2021.
- [50] Salma Abdel Magid, Yulun Zhang, Donglai Wei, Won-Dong Jang, Zudi Lin, Yun Fu, and Hanspeter Pfister. Dynamic high-pass filtering and multi-spectral attention for image super-resolution. In *Proceedings of the IEEE/CVF International Conference on Computer Vision*, pages 4288–4297, 2021.
- [51] Julia Grabinski, Steffen Jung, Janis Keuper, and Margret Keuper. Frequencylowcut pooling-plug and play against catastrophic overfitting. In *European Conference on Computer Vision*, pages 36–57. Springer, 2022.
- [52] Zhipeng Huang, Zhizheng Zhang, Cuiling Lan, Zheng-Jun Zha, Yan Lu, and Baining Guo. Adaptive frequency filters as efficient global token mixers. In *Proceedings of the IEEE/CVF International Conference on Computer Vision*, pages 6049–6059, 2023.
- [53] Lu Chi, Borui Jiang, and Yadong Mu. Fast fourier convolution. *Advances in Neural Information Processing Systems*, 33:4479–4488, 2020.
- [54] Yongming Rao, Wenliang Zhao, Zheng Zhu, Jiwen Lu, and Jie Zhou. Global filter networks for image classification. *Advances in neural information processing systems*, 34:980–993, 2021.
- [55] Zongyi Li, Nikola Kovachki, Kamyar Azizzadenesheli, Burigede Liu, Kaushik Bhattacharya, Andrew Stuart, and Anima Anandkumar. Fourier neural operator for parametric partial differential equations. *arXiv preprint arXiv:2010.08895*, 2020.
- [56] John Guibas, Morteza Mardani, Zongyi Li, Andrew Tao, Anima Anandkumar, and Bryan Catanzaro. Adaptive fourier neural operators: Efficient token mixers for transformers. *arXiv preprint arXiv:2111.13587*, 2021.
- [57] Linwei Chen, Ying Fu, Kaixuan Wei, Dezhi Zheng, and Felix Heide. Instance segmentation in the dark. *International Journal of Computer Vision*, 131(8):2198–2218, 2023.
- [58] Cheng Luo, Qinliang Lin, Weicheng Xie, Bizhu Wu, Jinheng Xie, and Linlin Shen. Frequency-driven imperceptible adversarial attack on semantic similarity. In *Proceedings of the IEEE/CVF conference on computer vision and pattern recognition*, pages 15315–15324, 2022.
- [59] Shuai Jia, Chao Ma, Taiping Yao, Bangjie Yin, Shouhong Ding, and Xiaokang Yang. Exploring frequency adversarial attacks for face forgery detection. In *Proceedings of the IEEE/CVF Conference on Computer Vision and Pattern Recognition*, pages 4103–4112, 2022.
- [60] Debapriya Sengupta, Phalguni Gupta, and Arindam Biswas. An efficient method for computation of entropy and joint entropy of images. In De-Shuang Huang, Vitoantonio Bevilacqua, and Abir Hussain, editors, *Intelligent Computing Theories and Application*, pages 282–290, Cham, 2020. Springer International Publishing.
- [61] Gwanggil Jeon. Information entropy algorithms for image, video, and signal processing. *Entropy*, 23(8), 2021.
- [62] Amelia Carolina Sparavigna. Entropy in image analysis. *Entropy*, 21(5), 2019.
- [63] Robert M. Haralick and Linda G. Shapiro. Image segmentation techniques. *Computer Vision, Graphics, and Image Processing*, 29(1):100–132, 1985.
- [64] Shraddha Tripathi, Krishna Kumar, BK Singh, and RP Singh. Image segmentation: A review. *International Journal of Computer Science and Management Research*, 1(4):838–843, 2012.
- [65] Dosovitskiy Alexey. An image is worth 16x16 words: Transformers for image recognition at scale. *arXiv preprint arXiv: 2010.11929*, 2020.
- [66] Yonghao Huang, Chuan Zhou, Leiting Chen, Junjing Chen, and Shanlin Lan. Medical frequency domain learning: Consider inter-class and intra-class frequency for medical image segmentation and classification. In *2021 IEEE International Conference on Bioinformatics and Biomedicine (BIBM)*, pages 897–904. IEEE, 2021.
- [67] Kaiming He, Georgia Gkioxari, Piotr Dollár, and Ross Girshick. Mask r-cnn. In *Proceedings of the IEEE international conference on computer vision*, pages 2961–2969, 2017.
- [68] Xi Chen, Zhiyan Zhao, Feiwu Yu, Yilei Zhang, and Manni Duan. Conditional diffusion for interactive segmentation. In *Proceedings of the IEEE/CVF International Conference on Computer Vision*, pages 7345–7354, 2021.
- [69] Qin Liu, Zhenlin Xu, Yining Jiao, and Marc Niethammer. isegformer: interactive segmentation via transformers with application to 3d knee mr images. In *International Conference on Medical Image Computing and Computer-Assisted Intervention*, pages 464–474. Springer, 2022.
- [70] Minghao Zhou, Hong Wang, Qian Zhao, Yuexiang Li, Yawen Huang, Deyu Meng, and Yefeng Zheng. Interactive segmentation as gaussian process classification. In *Proceedings of the IEEE/CVF Conference on Computer Vision and Pattern Recognition*, pages 19488–19497, 2023.
- [71] Yian Zhao, Kehan Li, Zesen Cheng, Pengchong Qiao, Xiaowu Zheng, Rongrong Ji, Chang Liu, Li Yuan, and Jie Chen. Graco: Granularity-controllable interactive segmentation. In *Proceedings of the IEEE/CVF Conference on Computer Vision and Pattern Recognition (CVPR)*, pages 3501–3510, June 2024.
- [72] Ke Sun, Yang Zhao, Borui Jiang, Tianheng Cheng, Bin Xiao, Dong Liu, Yadong Mu, Xinggang Wang, Wenyu Liu, and Jingdong Wang. High-resolution representations for labeling pixels and regions. *arXiv preprint arXiv:1904.04514*, 2019.
- [73] Diederik P Kingma. Adam: A method for stochastic optimization. *arXiv preprint arXiv:1412.6980*, 2014.
- [74] Kaiming He, Xiangyu Zhang, Shaoqing Ren, and Jian Sun. Deep residual learning for image recognition. In *Proceedings of the IEEE conference on computer vision and pattern recognition*, pages 770–778, 2016.
- [75] Ze Liu, Yutong Lin, Yue Cao, Han Hu, Yixuan Wei, Zheng Zhang, Stephen Lin, and Baining Guo. Swin transformer: Hierarchical vision transformer using shifted windows. In *Proceedings of the IEEE/CVF*

*international conference on computer vision*, pages 10012–10022, 2021.

- [76] Alexey Dosovitskiy, Lucas Beyer, Alexander Kolesnikov, Dirk Weissenborn, Xiaohua Zhai, Thomas Unterthiner, Mostafa Dehghani, Matthias Minderer, Georg Heigold, Sylvain Gelly, et al. An image is worth 16x16 words: Transformers for image recognition at scale. *arXiv preprint arXiv:2010.11929*, 2020.